Observation of Symmetry-Broken Hyperbolic Polaritons at Nanoscale

Guangwei Hu[1,†], Weiliang Ma[2,†], Debo Hu[3,†], Jing Wu[4], Chunqi Zheng[1,5], Kaipeng Liu[1], Xudong Zhang[6], Xiang Ni[7], Jianing Chen[8], Xinliang Zhang[2], Qing Dai[3,*], Joshua D. Caldwell[9], Alexander Paarmann[10], Andrea Alù[7, 11,*], Peining Li[2,*], Cheng-Wei Qiu[1,5, *]

1 Department of Electrical and Computer Engineering, National University of Singapore, Singapore
2 Wuhan National Laboratory for Optoelectronics and School of Optical and Electronic Information, Huazhong University of Science and Technology, Wuhan, China
3 CAS Key Laboratory of Nanophotonic Materials and Devices, CAS Key Laboratory of Standardization and Measurement for Nanotechnology, CAS Center for Excellence in Nanoscience, National Center for Nanoscience and Technology, Beijing, China
4 Institute of Materials Research and Engineering, Agency for Science, Technology and Research, Singapore
5 NUS Graduate School, National University of Singapore, Singapore
6 Ministry of Industry and Information Technology Key Lab of Micro-Nano Optoelectronic Information System, Harbin Institute of Technology, Shenzhen, China,
7 Photonics Initiative, Advanced Science Research Center, City University of New York, New York, NY, USA
8 Institute of Physics, Chinese Academy of Sciences, 100190 Beijing, China
9 Department of Mechanical Engineering, Vanderbilt University, Nashville, TN, USA
10 Fritz Haber Institute of the Max Planck Society, Berlin, Germany
11 Physics Program, Graduate Center, City University of New York, New York, NY, USA

* Correspondence to: daiq@nanoctr.cn; aalu@gc.cuny.edu; lipn@hust.edu.cn; chengwei.qiu@nus.edu.sg
† these authors contributed equally: Guangwei Hu, Weiliang Ma, Debo Hu

Various optical crystals possess permittivity components of opposite signs along different principal directions in the mid-infrared regime, exhibiting exotic anisotropic phonon resonances. Such materials support hyperbolic polaritons, hybrid light-matter quasiparticles with open isofrequency contours, feature large momenta optical modes and wave confinement and hold the promise for novel nanophotonic on-chip technologies[1-5]. Most studies thus far have focused on crystals with high symmetry in which the involved phonon vibrations obey certain propagation patterns, including hexagonal (boron nitride)[6], trigonal ($CaCO_3$)[7] and orthorhombic (α-MoO_3 or α-V_2O_5)[8-13] materials. Lower-symmetry materials such as the monoclinic crystals were recently demonstrated to offer richer opportunities for novel polaritonic phenomena[14, 15]. Here, we report direct real-space nanoscale imaging of symmetry-broken hyperbolic phonon polaritons in monoclinic $CdWO_4$ crystals, and showcase inherently asymmetric polariton excitation and propagation using scanning near-field optical microscopy. We also present a quantitative recipe to describe the polariton asymmetry and schemes to enhance the asymmetry via damping loss of phonon modes and further theoretically explains its origins. Our findings unlock new possibilities for polaritonics in natural materials with lower symmetries, ideally favoring versatile and extreme manipulation of light at the nanoscale for infrared nanophotonics.

Optical anisotropic behaviors are an important feature of natural optical materials in the context of crystal optics[16]. Recently, extreme optical anisotropy - in the form of hyperbolic responses - has been identified in various polar crystals, for which the permittivity components along different principal directions of the crystals show different signs. When interacting with light, such polar materials may yield hyperbolic phonon polaritons (HPhPs), i.e., quasiparticles of coupled light and infrared-active optical phonons with hyperbolic dispersion. These polaritons exhibit low loss[17] and strong wave confinement associated with their large momenta[18,19], thus enhancing light-matter interactions[20] and allowing directional control of energy flow[21] at the nanoscale for applications such as infrared sensing[22, 23], subdiffractive imaging[24-26], and

photodetection[27] to name a few. Various materials supporting this response have been studied, from van der Waals thin films[5] including hexagonal boron nitride (hBN)[6], alpha-phase molybdenum trioxide (α-MoO_3)[8-10], alpha-phase vanadium pentoxide (α-V_2O_5)[13], anisotropic bulk crystals such as calcite[7] and β-gallium oxide[15].

In crystallography, most of these anisotropic media are categorized as hexagonal (hBN, see **Figure 1a**), trigonal ($CaCO_3$, rhombohedral) and orthorhombic (α-V_2O_5, α-MoO_3, see **Figure 1b**) crystals. They demonstrate higher symmetry compared to low-symmetry crystals (LSCs) such as monoclinic (**Figure 1c**) and triclinic lattices[28, 29]. Monoclinic crystals, in particular, are characterized by unequal lengths of their three principal axes. In addition, they support only two-fold axis of rotational symmetry along $\mathbf{a_2}$, and a mirror plane ($\mathbf{a_1}$-$\mathbf{a_3}$ plane), but their $\mathbf{a_1}$ and $\mathbf{a_3}$ axes are non-orthogonal (**Figure 1c**). Such reduced symmetry introduces challenges for some optical applications, but at the same time offers an interesting "knob" for fine phase and polarization control of light propagation [14]. The impact of the low structural symmetry upon the polaritonic response at the deeply subwavelength scale has only recently been investigated, resulting in the observation of so-called shear polaritons whereby both the momentum (wavelength) and propagation direction disperse with frequency[15]. Nevertheless, a direct real-space observation of polariton propagation in LSCs as well as full modelling of exotic surface modes could complement the understanding of the impact of such low symmetry on polariton propagation.

In this paper, we discuss the role of lower crystal symmetry on the generation and propagation of shear hyperbolic phonon polaritons, and report their near-field real-space observation in monoclinic cadmium tungstate ($CdWO_4$), a LSC well-known for its application in scintillation detectors [30]. The real-space nanoimaging of polaritons at the surface of $CdWO_4$ is achieved by scattering-type scanning near-field optical microscopy (s-SNOM), revealing hyperbolic polariton wavefronts with asymmetric propagation signatures. Such asymmetry fundamentally originates from the fact that the non-Hermitian permittivity tensor cannot be diagonalized in real space as interpreted by our theory (see Supplementary Section 1). Our results suggest that LSCs naturally facilitate additional degrees of freedom to mold the interfacial flow of light at nanoscale.

We first present the unique impact of crystal symmetry on their optical response. A crystal with hexagonal lattice supports degenerate optical phonons oscillating in the plane, which implies the presence of in-plane isotropic polariton propagation in hBN[6, 31] (**Figure 1d**). For orthorhombic lattices, non-degenerate dipolar excitations of phonon resonances can exist with different strengths due to inequal lattice constants, thus offering in-plane anisotropy in α-MoO_3 [8,9] and α-V_2O_5[13] (**Figure 1e**). In contrast, multiple dipolar excitations in the form of optical phonons in LSCs will not necessarily be orthogonal to one another (**Figure 1f**), due to the low crystal symmetry and anharmonic lattice vibrations[32]. To consider the dielectric response of optical crystals, each optical phonon mode contribute to the permittivity tensor as a Lorentz oscillator (denoted as φ_l where subscript integer l denotes the mode index) with the auxiliary freedom of their angular orientation (γ_l), see Methods. Here, due to the orthogonality of those phonon modes in hexagonal, trigonal and orthorhombic crystals, γ_l is either 0 or 90 degrees, which hence is usually overlooked. However, in LSCs, γ_l can be nearly arbitrary, offering a new degree of freedom for controlling the optical response and light propagation. Hence, four independent components of the permittivity tensor arise in LSCs, written in Cartesian coordinates as

$$\bar{\bar{\varepsilon}} = \begin{bmatrix} \varepsilon_{xx} & \varepsilon_{xy} & 0 \\ \varepsilon_{yx} & \varepsilon_{yy} & 0 \\ 0 & 0 & \varepsilon_{zz} \end{bmatrix}$$

where $\varepsilon_{xy} = \varepsilon_{yx}$ as bounded by reciprocity. Since all these dispersive components are complex-valued entries, so this is a non-Hermitian tensor [14]. Importantly, when $\bar{\bar{\varepsilon}}$ is non-diagonalizable in the reals using unitary rotation matrices, we could obtain the symmetry-broken polaritons (see Methods and Supplementary Section 1 and 2).

To directly visualize the effect of such low symmetry on the nanoscale propagation of light, we first consider a crystal with two non-orthogonal, non-degenerate (i.e., different oscillation eigen-frequencies) optical phonons with different orientations (with angle $\Delta\gamma = \gamma_2 - \gamma_1$, while $\gamma_1 \overset{\text{def}}{=} 0$, see note 2 in section 1 of Supplementary Informtaion) and performed full-wave numerical finite-element simulations to examine dipole-launched polaritonic modes (see Methods). We fixed the frequency at 870 cm^{-1}. The field at the top surface of $\mathbf{a_1}$-$\mathbf{a_3}$ plane is shown in **Figure 1g-j**. When $\Delta\gamma = 0°$ (**Figure 1g**) or 90° (**Figure 1j**), the polaritons at the interface are symmetric with respect to two optic axes (along *x* and *y* directions), showing a hyperbolic dispersion in the Fourier spectrum (Fourier transform, FT, of the field). However, for different angles, we find asymmetric propagation of polaritons with respect to the effective optic axis and different open directions when $\Delta\gamma = 30°$ (**Figure 1h**), which becomes more pronounced when $\Delta\gamma = 60°$ (**Figure 1i**). Here, the two effective optic axis (O1 and O2) are in the plane and, by our definition, along the directions where the real part of permittivity tensor can be diagonalized (see see note 1 in section 1 of Supplementary Informtaion), which provides the symmetric responses if loss is neglected. The fundamental mechanism is the excitation of asymmetric hyperbolic polaritons, as shown in their FT spectrum, due to the non-orthogonality of the two underlying phonon modes, which we will discuss in more details later. This evidence points to the fact that LSCs offer a new platform for extreme manipulation of the flow of polaritons and energy.

To map such asymmetric dispersion of hyperbolic shear phonon polaritons, we performed s-SNOM at the (010) surface of $CdWO_4$ crystal. $CdWO_4$ crystal has monoclinic symmetry with space group 13 (*P*12 / *C*1), which supports 8 optically active non-orthogonal optical phonons (B_u symmetry) with polarization in the $\mathbf{a_1}$-$\mathbf{a_3}$ plane and 7 phonons modes (Au symmetry) with polarization along $\mathbf{a_2}$ directions[30]. We denote their orientation anglesof the induced polarization as γ_l (l=1, 2, … 8 from high to low frequency), which are all different (see specific values provided in Table of Supplementary Section 1). In our sample, the eigen-displacements of those optical phonons of interest are within the $CdWO_4$/air interface, which is ideal for s-SNOM nanoimaging. We define the x direction along $\mathbf{a_1}$ of the atomic unit cell and the normal direction of this interface as *z* (which is parallel to **a2** direciton). The sample thickness is 5 mm with surface dimensions of 5x5 mm, much larger than the operating wavelength of interest. Thus, we can reasonably regard the sample to be semi-infinite. We fabricated gold disks (diameter ~ 1 μm) on the surface of $CdWO_4$. As shown in **Figure 2a**, when illuminating a laser beam with *p*-polarized mid-infrared light onto the disk (E_{in}), it will act as an optical antenna launching polaritons (E_p) propagating along the surface, which would be picked up by the tip of s-SNOM. Note that we well align the illumination direction along the O1 axis (with an incident angle of 30°) to avoid any illumination-caused asymmetry in the direction parallel to the O2 axis.

For our experimental measurements, we focus on phonon polaritons in the infrared restrstrahlen band (RB) within the spectral range from 780 cm^{-1} to 901 cm^{-1} (as limited by our laser

source in the experimental setup), while other optical phonons, neither orthogonal nor parallel to these phonons, and the induced polarization from $\bar{\bar{\varepsilon}}_{\infty}$ term contribute to the asymmetry (see Note 5 in section 1 of Supplementary Information and Supplementary Figure 5). The near-field ampltitude image at ω=870 cm^{-1} is presented in **Figure 2b,** showing long (over 5 μm) and ray-like polariton propagation. The Fourier spectrum of near-field images is exhibited in **Figure 2c**, demonstrating in-plane hyperbolic characteristics. These observations agree well with numerical simulations (see Supplementary Figure 6), verifying in-plane hyperbolic responses of $CdWO_4$ polaritons and suggesting the capability of strong confinement of light at nanoscale due to the unbounded open dispersion contours. We attribute the vertical bright lines in near-field singals as the noise.

More important is that the observed polariton patterns are asymmetric with respect to both the O1 and O2 axes. We attribute the asymmetry with respect to the O2 axis to the oblique illumination[33], similar to the recent experimental observation of polaritons in calcite[7]. Interestingly, an additional asymmetry with respect to the O1 axis is observed: the polaritonic rays notably decay faster on the upper right side of the O1 axis than to the lower right side (**Figure 2b** and see analysis of line-cut signals in supplementary Figure S7). Such asymmetry is absent in calcite polaritons because the mirror symmetry in trigonal crystals guarantees the symmetric excitation of polaritons with respect to the plane containing the optic axis and normal direction of the interface. Hence, our observed symmetry breaking with respect to O1 axis is an intrinsic property of LSC with broken mirror symmetry and hence independent of the illumination, because we fixed the illumination direction in the measurements to be parallel to the O1 axis. The asymmetry is also reflected in the Fourier transform analysis of the near-field images (**Figure 2c**), namely, when $k_{O1}>0$, the upper isofrequency curve ($k_{O2}>0$) is shorter than the lower branch ($k_{O2}<0$). These landmark observations support that monoclinic $CdWO_4$ can indeed render the low-symmetry polaritons, predicted by our theoretical calculation of dispersion (**Figure 2d** and supplementary Figure 8), which will be discussed in details later.

Such asymmetric propagation of polaritons is robust, and, in order to confirm this feature, we measured the polaritons at other frequencies including ω=865 cm^{-1} (**Figure 3a**), ω=875 cm^{-1} (**Figure 3b**), and ω=880 cm^{-1} (**Figure 3c**). The corresponding Fourier spectra are shown in **Figure 3d-f**, respectively, all exhibiting asymmetry. Although these measurements are in the same RB, we note that asymmetric hyperbolic polaritons are predicted to also arise in other RBs, as shown in theoretical calculations provided in Supplementary Figure 4 and 5. In addition, the open direction of hyperbolic dispersion changes with respect to the operation frequency in different RBs (see both numerical and experimental demonstrations in Supplementary Section 1 and Suppmentary Figure 2 and 3), and sometimes even noticeable within the same RB (see Supplementary Figure 4 and 5). To summarize, the extreme anisotropy, symmetry breaking and dispersion of optic axis are three distinguished features of LSC, unattainable in tetragonal, trigonal, hexagonal or orthorhombic systems with higher symmetry.

The demonstrated symmetry breaking can be further enhanced. The polariton asymmetry essentially stems from the non-diagonalizability of a complex permittivity tensor in the reals[14] due to non-orthogonal phonon modes, as illustrated in **Figure 1** and attested by our experiments. It is worth noting that the damping loss of each individual mode plays an important role, as it can modify the extent of how such complex permittivity tensor deviates from being diagonalized in real space. Such derivation is quantitatively measured as an $\mathcal{M}$ value, where the larger value refers to the lower symmetry (see Methods and Supplementary Section 2). We thus start from the case study of **Figure**

1i, which corresponds to the orientation angle $\Delta\gamma = 60°$ and frequency ω=870 cm^{-1}, and alter $\mathcal{M}$ via tuning the damping loss of one phonon mode (S_1) to check how the polariton asymmetry will change. We performed numerical simulations using a dipole to excite the hyperbolic shear polaritons in the crystal and rigorously derive the dispersion of the polariton modes. The numerical field distribution is shown in **Figure 4a-c**, in which three different damping levels are considered: S_1= 10 cm^{-1} ($\mathcal{M}$=0.0011, **Figure 4a**), S_1=30 cm^{-1} ($\mathcal{M}$=0.0263, **Figure 4b**) and S_1=50 cm^{-1} ($\mathcal{M}$=0.0808, **Figure 4c**), respectively. One can clearly observe that the field distribution becomes increasingly asymmetric with respect to the O1 axis, in accordance with their Fourier spectra displayed in **Figure 4d-f**. Besides, since we have $\mathcal{M}$=0.0186 in **Figure 1i**, we indeed can visualize that the asymmetry in **Figure 4b,c** is stronger than that in **Figure 1i** while the asymmetry in **Figure 4a** is weaker than that in **Figure 1i**. Those observations suggest a possible route to quantitatively measure the degree of asymmetry with our method. We anticipate such avenue to enhance the asymmetry can be realized via reducing the isotope purity or increasing the working temperature of LSCs, that may increase the dampings of the ossocaited phonon modes, which could be experimentally explored in the future.

In the end, we discuss the physical origins behind this asymmetry. It is known that resonant modes at the interface correspond to poles of the dyadic Green's function of the system, which arises when the transverse impedances in the two media are opposite to each other. In our case, we denote the transverse wave impedance of the isotropic dielectric background as $\eta_d \propto k_z^d$ (where $k_z^d = \sqrt{\varepsilon_d - k_\rho^2}$ is the momentum along z direction in the background with dielectric constant ε_d) and in the anisotropic crystal as $\eta_c \propto \frac{1}{k_z}$ (where k_z is the momentum along z direction of optical crystals). The transverse resonance condition requires $\eta_d + \eta_c = 0$ (see detailed deriviation in Supplementary Section 3). Since η_d does not depend on the in-plane direction of interest due to the material isotropy, we examine the η_c component. For this purpose, we show k_z of the crystal as contour line plots in **Figure 4d-f**, where the red and green dashed lines denote Re[k_z] and Im[k_z], respectively. In **Figure 4d**, one can find that the resonant modes and k_z distribution are nearly symmetric with respect to the O1 axis. However, when the symmetry is broken for higher damping, we do observe a pronounced asymmetry in the dispersion plot of k_z in **Figure 4e,f**. Such distorted momenta suggest the asymmetric transverse resonance at the interface, which is, for a particular point in the momentum space where the wave impedance matching condition is reached, its mirror point with respect to O1 axis will automatically not satisfy this matching condition due to the asymmetry of solution k_z. Consequently, the broken-symmetric polariton propagation is rendered at two sides of O1 axis (**Figure 4b,c**). Our interpretation is further supported by the agreement between the numerically obtained Fourier spectra and our analytical calculations shown in **Figure 4g-i**. We note that this asymmetric resonance condition also explains our experimental observation of asymmetric $CdWO_4$ polaritons, as shown by different resonant amplitudes of the reflection coefficient in **Figure 2d**, which can be further enhanced if the distortion of k_z is more pronounced (**Supplementary Figure 9**). This model is applicable to other scenarios regardless of material loss and frequency dispersion. Hence, this can be readily extended to other monoclinic crystals and triclinic systems with even lower symmetry.

In this work, we studied asymmetric HPhPs in LSC with an exemplary monoclinic crystal $CdWO_4$. Combined with rigorous theoretical investigations, we provided direct real-space nanoimaging of rotating and asymmetric polaritons. Essentially, the reduced symmetry of LSCs stems from the non-diagonalizability of complex permittivity tensors in real space, which renders

the distorted dissipation and underpins extreme asymmetric propagation of shear polaritons. Such LSCs therefore provide an ideal and naturaly occurring paradigm to non-Hermitian photonics. Moreover, the study of natural LSCs will further inspire its meta-photonics and meta-optics[34]. Our findings with tailorable symmetry-broken hyperbolic polaritons in bulk crystals will be important and readily valuable for various technologies such as infrared sensing, super-Planckian heat emission, near-field radiation management, photonic circuits and many others.

Reference:

1. Caldwell, J. D. et al. Low-loss, infrared and terahertz nanophotonics using surface phonon polaritons. *Nanophotonics* **4**, 44–68 (2015).
2. Basov, D. N., Fogler, M. M. & García de Abajo, F. J. Polaritons in van der Waals materials. *Science* **354**, aag1992 (2016).
3. Low, T. et al. Polaritons in layered two-dimensional materials. *Nat. Mater*. **16**, 182–194 (2017).
4. Hu, G., Shen, J., Qiu, C.-W., Alù, A. & Dai, S. Phonon polaritons and hyperbolic response in van der Waals materials. *Adv. Opt. Mater*. **8**, 1901393 (2020).
5. Zhang, Q. et al. Interface nano-optics with van der Waals polaritons. *Nature* **597**, 187–195 (2021).
6. Dai, S. et al. Tunable phonon polaritons in atomically thin van der Waals crystals of boron nitride. *Science* **343**, 1125–1129 (2014).
7. Ma, W. et al. Ghost hyperbolic surface polaritons in bulk anisotropic crystals. *Nature* **596**, 362-366 (2021).
8. Zheng, Z. et al. Highly confined and tunable hyperbolic phonon polaritons in van der Waals semiconducting transition metal oxides. *Adv. Mater*. **30**, e1705318 (2018).
9. Ma, W. et al. In-plane anisotropic and ultra-low-loss polaritons in a natural van der Waals crystal. *Nature* **562**, 557–562 (2018).
10. Hu, G. et al. Topological polaritons and photonic magic angles in twisted α-MoO_3 bilayers. *Nature* **582**, 209–213 (2020).
11. Duan, J. et al. Twisted Nano-Optics: Manipulating Light at the Nanoscale with Twisted Phonon Polaritonic Slabs. *Nano Lett.* **20**, 5323-5329 (2020).
12. Zheng, Z. et al. Phonon Polaritons in Twisted Double-Layers of Hyperbolic van der Waals Crystals. *Nano Lett.* **20**, 5301-5308 (2020).
13. Taboada-Gutiérrez, J. et al. Broad spectral tuning of ultra-low-loss polaritons in a van der Waals crystal by intercalation. *Nat. Mater*. **19**, 964–968 (2020).
14. Schubert, M. et al.,. Anisotropy, phonon modes, and free charge carrier parameters in monoclinic β-gallium oxide single crystals. *Phys. Rev. B* 93, 125209 (2016).
15. Passler, N. et al., Hyperbolic Shear Polaritons in Low-Symmetry Crystals. *Nature* **602**, 595–600 (2022).
16. Born, M. & Wolf, E. *Principles of Optics* 5th edn 333–334 (Pergamon, Oxford, 1975).
17. Giles, A. J. *et al.* Ultralow-loss polaritons in isotopically pure boron nitride. *Nat. Materials* **17**, 134-139 (2018).

18. I.-H. Lee *et al.*, Image polaritons in boron nitride for extreme polariton confinement with low losses. *Nat. Commun.* **11**, 3649 (2020);
19. Ambrosio, A. et al. Selective excitation and imaging of ultraslow phonon polaritons in thin hexagonal boron nitride crystals. *Light Sci. Appl.* **7**, 27 (2018).
20. P. Li *et al.*, Collective near-field coupling and nonlocal phenomena in infrared-phononic metasurfaces for nano-light canalization. *Nat. Commun.* **11**, 3663 (2020).
21. K.-J. Tielrooij *et al.*, Out-of-plane heat transfer in van der Waals stacks through electron–hyperbolic phonon coupling. *Nat. Nanotechnol.* **13**, 41-46 (2018).
22. Autore, M. et al. Boron nitride nanoresonators for phonon-enhanced molecular vibrational spectroscopy at the strong coupling limit. *Light Sci. Appl*. **7**, 17172 (2018).
23. Bylinkin, A. et al. Real-space observation of vibrational strong coupling between propagating phonon polaritons and organic molecules. *Nat. Photon*. **15**, 197–202 (2021).
24. Li, P. et al. Hyperbolic phonon-polaritons in boron nitride for near-field optical imaging and focusing. *Nat. Commun*. **6**, 7507 (2015).
25. Caldwell, J. D. et al. Sub-diffractional volume-confined polaritons in the natural hyperbolic material hexagonal boron nitride. Nature Commun. 5, 5221 (2014).
26. Feres, F.H., Mayer, R.A., Wehmeier, L. *et al.* Sub-diffractional cavity modes of terahertz hyperbolic phonon polaritons in tin oxide. *Nat Commun* **12,** 1995 (2021).
27. Castilla, S. *et al.* Plasmonic antenna coupling to hyperbolic phonon-polaritons for sensitive and fast mid-infrared photodetection with graphene. *Nat. Commun.* **11**, 4872 (2020).
28. Kittel, Charles, Paul McEuen, and Paul McEuen. Introduction to solid state physics. Vol. 8. New York: Wiley, 1996.
29. Landau, Lev Davidovich, et al. *Electrodynamics of continuous media*. Vol. 8. elsevier, 2
30. Gillette RH. Calcium and cadmium tungstate as a scintillation counter crystal for gamma-ray detection. *Rev Sci Instr* **21**, 294 (1950)
31. Caldwell, J. et al. Sub-diffractional volume-confined polaritons in the natural hyperbolic material hexagonal boron nitride. *Nat Commun* **5**, 5221 (2014).
32. Mock, A., Korlacki, R., Knight, S. and Schubert, M., Anisotropy, phonon modes, and lattice anharmonicity from dielectric function tensor analysis of monoclinic cadmium tungstate. *Phys. Rev. B* **95**, 165202 (2017)
33. Huber, A., Ocelic, N. & Hillenbrand, R. Local excitation and interference of surface phonon polaritons studied by near-field infrared microscopy. *J. Microsc.* **229**, 389-395 (2008).
34. Lee, D. et al. Hyperbolic metamaterials: fusing artificial structures to natural 2D materials. *eLight* 2, 1 (2022).

Methods

Permittivity of the $CdWO_4$ crystal

The permittivity tensor of the $CdWO_4$ crystal is calculated by Lorentz oscillator function with anharmonic broadening, where 8 Lorentz oscillators were used for calculating each component:

$$\varepsilon_{\mathrm{C}} = \begin{bmatrix} \varepsilon_{xx} & \varepsilon_{xy} & 0 \\ \varepsilon_{yx} & \varepsilon_{yy} & 0 \\ 0 & 0 & \varepsilon_{zz} \end{bmatrix}$$

$$\varepsilon_{xx} = \varepsilon_{xx,\infty} + \sum_{l=1}^{8} \varphi_l^{B_u} \cos^2 \gamma_l$$

$$\varepsilon_{xy} = \varepsilon_{yx} = \varepsilon_{xy,\infty} + \sum_{l=1}^{8} \varphi_l^{B_u} \sin \gamma_l \cos \gamma_l$$

$$\varepsilon_{yy} = \varepsilon_{yy,\infty} + \sum_{l=1}^{8} \varphi_l^{B_u} \sin^2 \gamma_l$$

$$\varepsilon_{zz} = \varepsilon_{zz,\infty} + \sum_{i=l}^{7} \varphi_l^{A_u}$$

$$\varphi_l = \frac{A_l^2 - i\omega\Gamma_l}{\omega_{\mathrm{TO},l}^2 - \omega^2 - i\omega S_l}$$

Here, ε_∞ is the high-frequency permittivity for all the phonon modes along different directions where $\varepsilon_{xx,\infty} = 4.46$, $\varepsilon_{yy,\infty} = 4.81$, $\varepsilon_{xy,\infty} = 0.086$ and $\varepsilon_{zz,\infty} = 4.25$; φ_l describes the contributions of each optical phonon oscillators; A_l, $\omega_{\mathrm{TO},l}$, Γ_l and S_l denotes the amplitude, TO phonon frequency, harmonic broadening and TO mode broadening of the associated harmonic oscillators. Here, γ_l is the unit vector orientation of eigen-displacement of the TO mode. All the parameters of each harmonic oscillators are from reference[32].

$\mathcal{M}$ factor for quantative measurement of asymmetry

The $\mathcal{M}$ factor as the quantity to measure the asymmetry is defined as

$$\mathcal{M}(\theta) = \frac{1}{\begin{vmatrix} \varepsilon_1 & 0 \\ 0 & \varepsilon_2 \end{vmatrix}} \left| \begin{pmatrix} \varepsilon_{xx} & \varepsilon_{xy} \\ \varepsilon_{xy} & \varepsilon_{yy} \end{pmatrix} - \begin{pmatrix} \varepsilon_1 \cos^2\theta + \varepsilon_2 \sin^2\theta & (\varepsilon_1 - \varepsilon_2)\sin\theta\cos\theta \\ (\varepsilon_1 - \varepsilon_2)\sin\theta\cos\theta & \varepsilon_1 \sin^2\theta + \varepsilon_2 \cos^2\theta \end{pmatrix} \right|$$

where the matrix $\begin{pmatrix} \varepsilon_1 & 0 \\ 0 & \varepsilon_2 \end{pmatrix}$ is the diagonalized matrix or eigenvalues of $\begin{pmatrix} \varepsilon_{xx} & \varepsilon_{xy} \\ \varepsilon_{xy} & \varepsilon_{yy} \end{pmatrix}$ using complex parameters. Hence, we have a mathematic problem to minimize the value of $\mathcal{M} = \min(M)$, with the respect of real parameters θ. More detailed derivation is shown in Supplementary Section II. For high-symmetry (hexagonal, orthorhombic, triagonal) crystal, one can mathematically prove that this quantity is zero. For monoclinic crystal, we can find that this is not always zero, due to non-diagonalizability of permittivity tensor in the real space. The larger the value of $\mathcal{M}$ is, the lower the symmetry. In our study, for example, in Figure 4 of main text, these values of $\mathcal{M}$ are 0.0011, 0.0263, and 0.0808, respectively, which hence have increasingly low symmetry.

Numerical simulation

A finite-element method using commercial software (COMSOL 5.6) are used to simulate near-field distributions of polaritons launched by vertical dipole. An electric dipole is placed 200 nm above

the surface of $CdWO_4$ crystal. The electric filed distribution (E_z) is recorded at 50 nm above the surface. A finite simulation range is 60*60μm is mostly used in our simulations, with scattering boundary conditions. The energy has been decayed significantly from this range, and the reflected field hence can be safely neglected. The simulation using larger areas are also used to confirm the field distribution.

Materials and fabrication

The $CdWO_4$ crystal with polished (010) surface is from the commercial company. The gold pattern on crystal surface is fabricated using electron-beam lithography following a lift-off process. The electron beam resist (ZEP 520, Zeon) was spin-coated on the sample, then baked for 10 min. A conductive polymer (AR-PC 5090.02, Allresist) was spin-coated on the resist to prevent charge accumulation. The pattern of the resistor was drawn on the resist by electron-beam lithography (Eline-plus). The sample was immersed in DI water for 1 min to remove the conductive polymer, then immersed in developing solution (N50:IPA=10:1, MACKLIN) for 1 min at 0 °C. A 100-nm thick gold layer is deposited on the sample by electron beam evaporation at 77 K refrigerated by liquid nitrogen. The deposition rate is fixed at 0.4 Å/s. A quick lift-off process was conducted to define Au pattern on the sample.

s-SNOM measurements

For the nanoimaging of polaritons in $CdWO_4$, we used a commercial s-SNOM system (Neaspec GmbH) coupled with the tunable quantum cascade laser (Daylight solution) with an operation frequency from 950 to 860 cm^{-1}. The infrared light illuminates a Pt-coated tip of an atomic force microscope (AFM) operating in the tapping mode. The tip oscillate vertically at a frequency $\Omega \approx$ 270 kHz and the oscillation amplitude is around 60 nm. The tip-scattered light is collected with a pseudo-heterodyne interferometer[35]. The background-free signal is demodulated at a higher harmonic $n\Omega (n \geq 2)$, yielding near-field amplitude s_n and phase φ_n images. Figs. 3 show amplitude s_2 images. The incident light is always oriented along the O1 axis of $CdWO_4$ crystal during all the measurements.

Reference

35. Ocelic, N., Huber, A. & Hillenbrand, R. Pseudoheterodyne detection for background-free near-field spectroscopy. *Appl. Phys. Lett.* **89**, 101124 (2006).

Competing interests:

The authors declare no competing financial interests.

Acknowledgements:

C.-W.Q. acknowledges the support from the National Research Foundation, Prime Minister's Office, Singapore, under its Competitive Research Programme (CRP award NRF CRP22-2019-0006) and from the grant (R-261-518-004-720) from Advanced Research and Technology Innovation Centre (ARTIC). Q.D. acknowledges the support from the National Natural Science Foundation of China (Grant No. 51925203). D.H. acknowledges the support from the National Natural Science Foundation of China (Grant No. 52072083). J.D.C. acknowledges financial support from the U.S. National Science Foundation (Grant No. 2128240). J. W. acknowledges the

Advanced Manufacturing and Engineering Young Individual Research Grant (AME YIRG Grant No. A2084c170) and SERC Central Research Fund (CRF). P.L. acknowledges the support from the National Natural Science Foundation of China (Grant No. 62075070).

Author contribution:

C.W. Q, P. L. and A. A. conceived the idea. G. H. and W. M. performed the theory, simulation and design, with significant input from C.W. Q. and A.A.. D. H. measured the sample with the supervision by P.L. and Q.D.. X.Z. fabricated the Au nanoantenna. G.H., W. M., J.C., A.P., Q. D., A.A., P. L. and C.W. analyzed the data, with the input of all other authors. G. H., W. M. and D. H. wrote the manuscript with significant contributions from all others. C.W. Q. oversaw the project.

Data and materials availability:

All data are available in the manuscript or the supplementary materials.

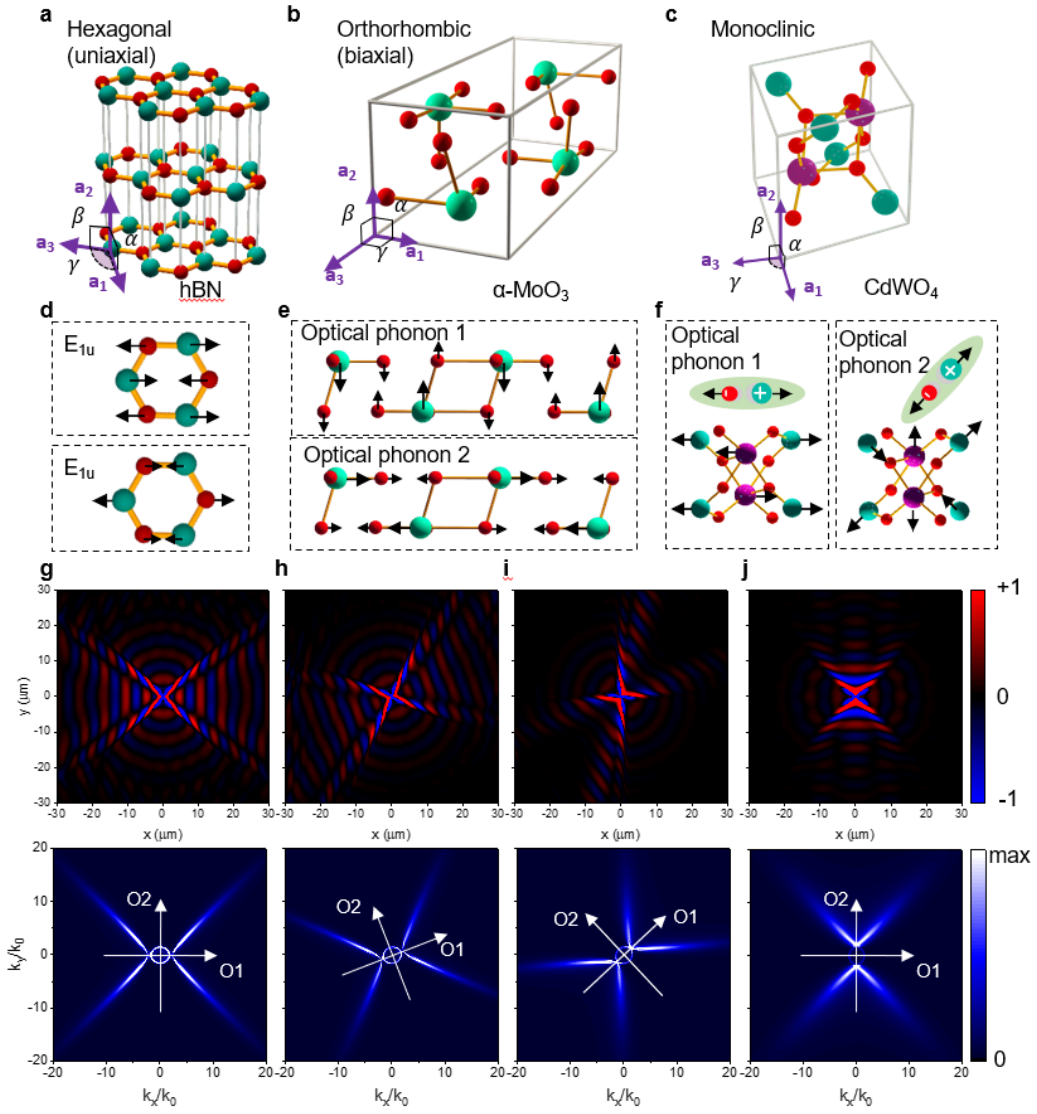

Figure 1 Hyperbolic polaritons in low-symmetry crystals. a, The hexagonal crystal in an example of hexagonal boron nitride (hBN) with uniaxial optical property. **b**, The orthorhombic α-MoO_3 crystal, featuring biaxial optical property. **c**, The monoclinic $CdWO_4$ crystal with lower symmetry. Here, three parameters $\mathbf{a_1}$, $\mathbf{a_2}$ and $\mathbf{a_3}$ denote vectors of unit cell, where the angle between them are dubbed α=< $\mathbf{a_1}$, $\mathbf{a_2}$>, β=< $\mathbf{a_2}$, $\mathbf{a_3}$> and γ=< $\mathbf{a_1}$, $\mathbf{a_3}$>. **d**, The eigen-displacement of degenerate E_{1u} phonon resonance in hexagonal crystals. **e**, The two eigen-displacement of ions for two transverse optical phonon in orthorhombic crystal, which are orthogonal. **f**, The schematic eigen-displacement for two non-degenerate transverse optical phonon in low-symmetry crystal. They in general can be induce two non-orthogonal dipolar resonance as schemed in the inset. Here, the black arrow denotes the displacement. **g-j**. The numerical field distribution (Re[Ez], top rows) and its corresponding hyperbolic dispersion (FFT, bottom rows) in low-symmetry crystal. Here, we vary the angle between two non-degenerate TO resonances to be 0° (panel g), 30° (panel h), 60° (panel i), and 90° (panel j). The working frequency is at 870cm^{-1}. The white arrowed lines in the panel show the directions of effective optical axis.

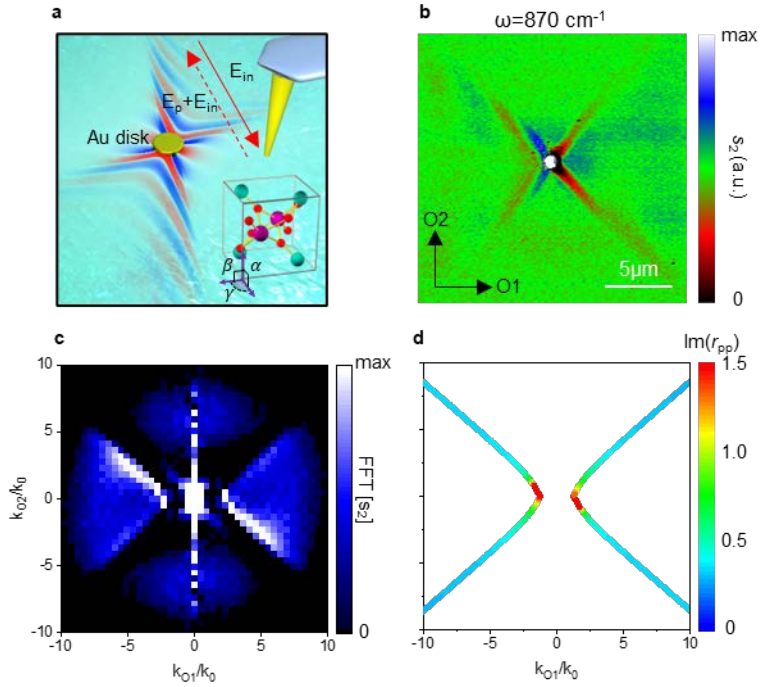

Figure 2 Near-field observation of polaritons in low-symmetry crystals. a, The schematic of scattering-type near-field mapping of hyperbolic phonon polaritons in $CdWO_4$. The crystal structure is shown in inset. The Au disk will serve as the nanoantenna to launch the polaritons, while the tip will record the Au-launched polariton (E_p) as well as the incident light (E_{in}). **b**, The measured near-field signals at the surface of CdWO4, at the frequency ω=870 cm^{-1}. Here, the lab coordinate is denoted as O1 and O2, the direction of two effective optic axis. **c**, The corresponding Fourier spectrum of measured near-field signals in panel **b**. **d**, The calculated dispersion, characterized by imaginary part of reflection coefficient.

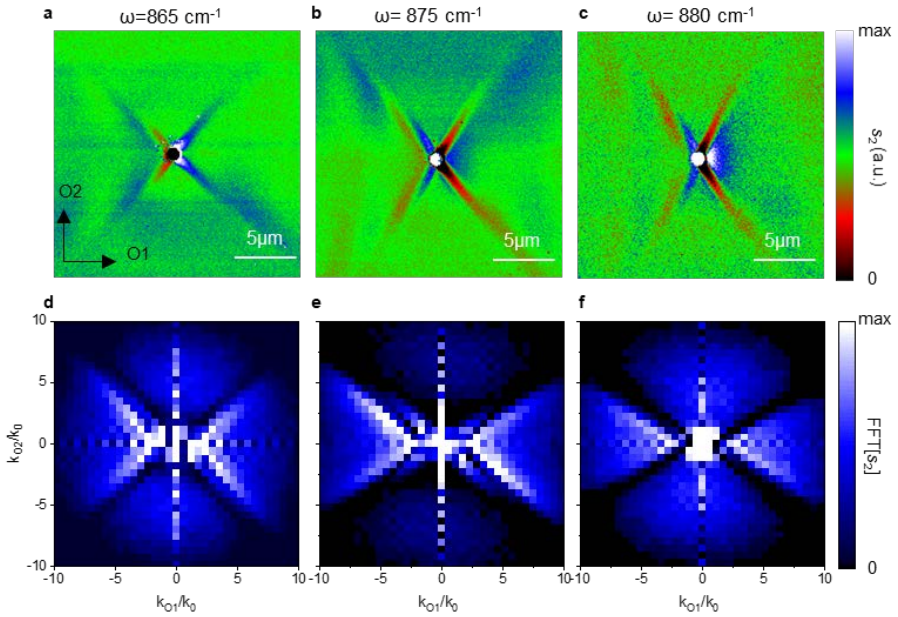

Figure 3 Near-field images of polaritons in low-symmetry $CdWO_4$ crystals. a-c, The measured near-field signals at the surface of CdWO4, at the frequency ω=865 cm^{-1} (panel a), ω=875 cm^{-1} (panel b), ω=880 cm^{-1} (panel c), respectively. **d-f**, The corresponding Fourier spectrum of measured signals.

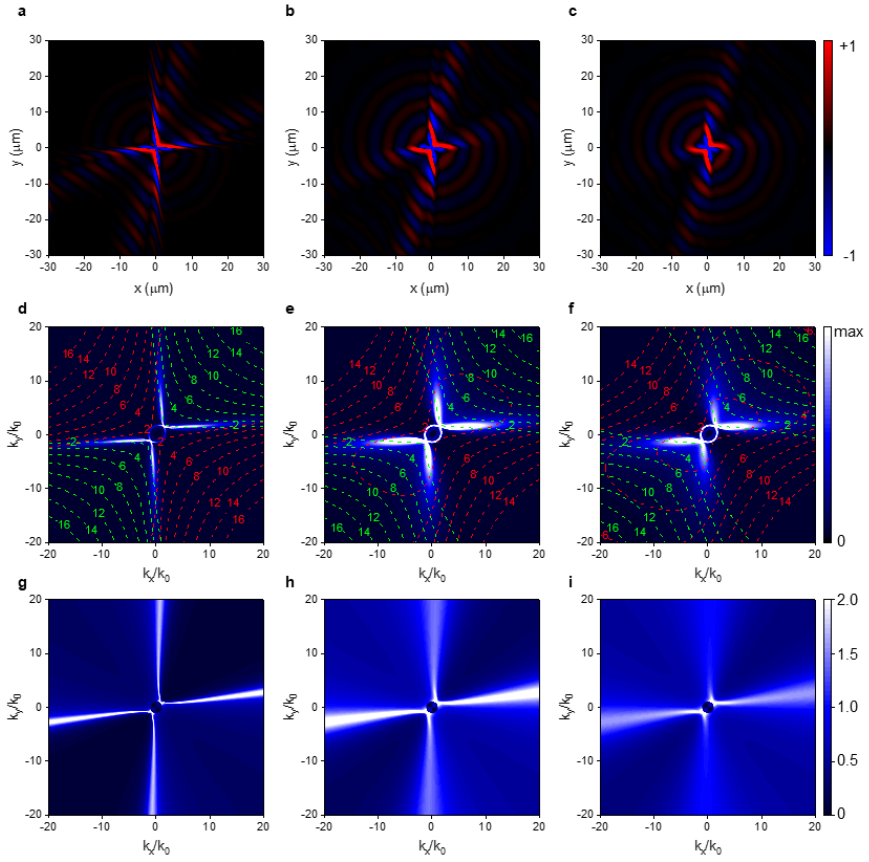

Figure 4 The symmetry-broken nature of hyperbolic polaritons in low-symmetry CWO crystals. a-c, The field distribution of dipole-launched polaritons at the 20 nm top of CWO sample at 870 cm^{-1}. Here, the permittivity tensor is obtained using two non-degenerate optical phonons, while varying the damping (S) of one mode: S_1=10 cm^{-1} (panel **a**), S_1=30 cm^{-1} (panel **b**) and S_1=50 cm^{-1} (panel **c**) respectively. **d-f.** Fourier spectra of the field distribution at panel **a-c** correspondingly. The red and green dashed contour lines mean the real and imaginary part of momentum along z direction (k_z) at the associated position of (k_x, k_y), correspondingly. **g-i**, the calculated dispersion of resonant mode at the surface for the case of panel **a-c**, respectively. Here, the colour contour is the imaginary part of reflection of TM polarized (denoted as "p") component at TM polarized incidence.

Supplementary Information

Observation of Symmetry-Broken Hyperbolic Polaritons at Nanoscale

Guangwei Hu[1,†], Weiliang Ma[2,†], Debo Hu[3,†], Jing Wu[4], Chunqi Zheng[1,5], Kaipeng Liu[1], Xudong Zhang[6], Xiang Ni[7], Jianing Chen[8], Xinliang Zhang[2], Qing Dai[3,*], Joshua D. Caldwell[9], Alexander Paarmann[10], Andrea Alù[7, 11,*], Peining Li[2,*], Cheng-Wei Qiu[1,5, *]

1 Department of Electrical and Computer Engineering, National University of Singapore, Singapore
2 Wuhan National Laboratory for Optoelectronics and School of Optical and Electronic Information, Huazhong University of Science and Technology, Wuhan, China
3 CAS Key Laboratory of Nanophotonic Materials and Devices, CAS Key Laboratory of Standardization and Measurement for Nanotechnology, CAS Center for Excellence in Nanoscience, National Center for Nanoscience and Technology, Beijing, China
4 Institute of Materials Research and Engineering, Agency for Science, Technology and Research, Singapore
5 NUS Graduate School, National University of Singapore, Singapore
6 Ministry of Industry and Information Technology Key Lab of Micro-Nano Optoelectronic Information System, Harbin Institute of Technology, Shenzhen, China,
7 Photonics Initiative, Advanced Science Research Center, City University of New York, New York, NY, USA
8 Institute of Physics, Chinese Academy of Sciences, 100190 Beijing, China
9 Department of Mechanical Engineering, Vanderbilt University, Nashville, TN, USA
10 Fritz Haber Institute of the Max Planck Society, Berlin, Germany
11 Physics Program, Graduate Center, City University of New York, New York, NY, USA

* Correspondence to: daiq@nanoctr.cn; aalu@gc.cuny.edu; lipn@hust.edu.cn; chengwei.qiu@nus.edu.sg
† these authors contributed equally: Guangwei Hu, Weiliang Ma, Debo Hu

Section 1: The dielectric permittivity model

Here, we discuss the permittivity tensor of the monoclinic crystal with the emphasis of specific $CdWO_4$ crystal. For this monoclinic crystal, the phonon vibration can occur within the $\mathbf{a_1}$-$\mathbf{a_3}$ plane, or parallel to the $\mathbf{a_2}$ axis. Each phonon mode is described as a Lorentz oscillator in the permittivity model. For the crystal orientation (010), the $\mathbf{a_2}$ axis is aligned along z direction. Thus, only four components of the dielectric permittivity tensor are non-zero: ε_{xx}, $\varepsilon_{xy} = \varepsilon_{yx}$, ε_{yy} and ε_{zz}. These components are also frequency-dispersive and follow the reciprocity. Considering the in-plane permittivity components, we thus have $[\bar{\bar{\varepsilon}}]_{xy} = \begin{bmatrix} \varepsilon_{xx} & \varepsilon_{xy} \\ \varepsilon_{xy} & \varepsilon_{yy} \end{bmatrix}$. In general, this matrix is non-Hermitian, and we cannot always diagonalize it using the real rotation matrix.

We now comment on how the permittivity tensor of monoclinic crystals differs from the high-symmetry crystal like orthorhombic (α-MoO_3). For orthorhombic crystal, $[\bar{\bar{\varepsilon}}]_{x'y'} = \begin{bmatrix} \varepsilon_{xx} & 0 \\ 0 & \varepsilon_{yy} \end{bmatrix}$. One can further perform coordinate transformation using rotation matrix such as $R(\theta) = \begin{bmatrix} \cos\theta & \sin\theta \\ -\sin\theta & \cos\theta \end{bmatrix}$ to obtain $[\bar{\bar{\varepsilon}}]_{xy} = R(-\theta)[\bar{\bar{\varepsilon}}]_{x'y'}R(\theta)$ in the formal coordinate xy plane that will also induce the off-diagonal terms. However, one would never have a real rotation matrix $[R(\theta)]$ for the in-plane permittivity tensor (generally complex) of monoclinic crystals to make the off-diagonal term zero, which underpins the symmetry breaking and sheared dissipation in the crystals, as will be discussed later.

Such low symmetry in monoclinic crystals will no longer force the effective direction of lattice vibrations orthogonal and create the different eigen-displacement directions for different optical phonons. For the interpretation of permittivity tensor in those crystals, we hence write that

$$\varepsilon_{\mathrm{C}} = \begin{bmatrix} \varepsilon_{xx} & \varepsilon_{xy} & 0 \\ \varepsilon_{xy} & \varepsilon_{yy} & 0 \\ 0 & 0 & \varepsilon_{zz} \end{bmatrix} \tag{1.a}$$

$$\varepsilon_{xx} = \varepsilon_{xx,\infty} + \sum_{l=1}^{8} \varphi_l^{B_u} \cos^2\gamma_l \tag{1.b}$$

$$\varepsilon_{xy} = \varepsilon_{xy,\infty} + \sum_{l=1}^{8} \varphi_l^{B_u} \sin\gamma_l \cos\gamma_l \tag{1.c}$$

$$\varepsilon_{yy} = \varepsilon_{yy,\infty} + \sum_{l=1}^{7} \varphi_l^{B_u} \sin^2\gamma_l \tag{1.d}$$

$$\varepsilon_{zz} = \varepsilon_{zz,\infty} + \sum_{i=l}^{8} \varphi_l^{A_u} \tag{1.e}$$

$$\varphi_l = \frac{A_l^2 - i\omega\Gamma_l}{\omega_{\mathrm{TO},l}^2 - \omega^2 - i\omega S_l} \tag{1.f}$$

Here, ε_∞ is the high-frequency permittivity where $\varepsilon_{xx,\infty} = 4.46$, $\varepsilon_{yy,\infty} = 4.81$, $\varepsilon_{xy,\infty} = 0.086$ and $\varepsilon_{zz,\infty} = 4.25$; φ describes the harmonic oscillators contributed by each phonon modes; A_l,

$\omega_{TO,l}$, Γ_l and S_l denotes the amplitude, TO phonon frequency, harmonic broadening and TO mode broadening of the associated harmonic oscillators. Here, γ_l is the unit vector orientation of eigen-displacement of the TO mode. The superscript of A_u and B_u denote the optical phonons out of the plane (along $\mathbf{a}_2$ axis) and in the plane ($\mathbf{a}_1$-$\mathbf{a}_3$ axis). In Table 1, we listed the γ_l of lattice vibration in xy plane. All the parameters of each harmonic oscillators are from reference[1]. We also showed the plot of each dispersive permittivity in Supplementary Figure 1.

Table 1: Relative direction of phonon vibration with B_u symmetry

RB mode	8	7	6	5	4	3	2	1
TO/LO (cm^{-1})	98.1 /117	149.1 /180	227.3 /243.5	265.2 /269.1	276.3 /369.8	450.6 /466.5	549.0 /754	779.5 /901.4
γ_l (°)	18.9	145.1	127.6	81.9	65.6	0.8	113.1	24.3

Here, γ_l is the vector direction of eigen-displacement of transverse optical phonons with B_u symmetry in each RB. The dataset is obtained from reference [1].

Note 1: Effective optic axis

Here, we discuss the effective optic axis. Traditionally, the optic axis is defined as the direction where the light experiences no birefringence in anisotropic crystals. In monoclinic crystals, such condition will never be fulfilled, because of the non-diagonalizability in the real space of the asscociated permittivity tensor. Since the loss is usually small in phonon polaritonic system, we define the effective optic axis as the angle in the rotation matrix given by the matrix that only contains the real part of permittivity of monoclinic $CdWO_4$. Hence there are two optic axes, denoted as O1 and O2. The direction O1 is along within [0, 90°) with respect to *x* axis ($\mathbf{a_1}$ unit cell axes), while O2 is the orthogonal direction of O1. O1 and O2 are within a1-a3 plane and hence perpendicular to the a2 axes. The specific angle of O1 within several selective RB ranges in Supplementary Figure 1.

One important feature of monoclinic crystals is that the direction of effective optic axis can change with respect to frequency, known as dispersion of optic axis [2]. To experimentally confirm the intrinsic dispersion of effective optic axis of $CdWO_4$ crystal, we performed polarization-resolved Fourier transform infrared (FTIR) spectroscopy (see Supplementary Figure 2a). The results of reflectivity spectrum are shown in Supplementary Figure 2b, agreeing with our theoretical calculations (see Supplementary Figure 3). Two broad peaks are observed, assigned to two infrared Reststrahlen bands, dubbed RB1 (the spectral range from 780 cm^{-1} to 901 cm^{-1}) and RB2 (from 549 cm^{-1} to 754 cm^{-1}). We further exploited six different linear polarization angles with interval of 30 degrees to measure the reflection from $CdWO_4$, showing a strong polarization dependence in both RBs. Specifically, in RB2, the reflectivity becomes smallest at 30° and largest at 120°. In striking contrast, a reverse trend is identified in RB1 from 780 cm^{-1} to 901 cm^{-1}, thus being the largest at 30° while smallest at 120°. The results for both frequencies manifest a bidirectional signature with two characteristic axes, agreeing well with the microscopic interpretation of quasi-orthogonal phonon vibration modes of RB1 and RB2 via density function theory calculations (see ref. 31 in main text). Our theoretical modelling well predicts the far-field characteristics of rotary broken-symmetric phonon polaritons in both bands. Theoretical analysis further reveals that, in low-frequency RBs, self-rotating orientations of effective optic axis can even be allowed within the same RB (see Supplementary Figure 4). Such rotary effective optic axis along the azimuthal direction suggests a new recipe for on-demand dispersion engineering of polaritons enabled by the

low symmetry, which is not available in high-symmetry crystals such as tetragonal, triagonal, hexagonal or orthorhombic systems.

Note 2: The permittivity tensor used in Figure 1 and Figure 4 in main text

To simplify the discussion in Figures 1 and 4 of main text, without losing the generality, we only consider the two relatively high-frequency phonon modes 1 and 2 of $CdWO_4$, while setting $\varepsilon_{xx,\infty} = \varepsilon_{yy,\infty} = 4.1$, $\varepsilon_{xy,\infty} = 0$, and ε_{zz}=-5, where the $\varphi_l = \frac{A_l^2 - i\omega\Gamma_l}{\omega_{TO,l}^2 - \omega^2 - i\omega S_l}$ for $l = 1$ and 2. Here, $A_1 = 908.1$, $\Gamma_1 = 31.1$, $S_1 = 15.01$; and $A_2 = 1018.1$, $\Gamma_2 = -22.2$, $S_2 = 15.31$ (those units are cm^{-1}). The orientation angle $\gamma_1 \stackrel{def}{=} 0$ and angle $\Delta\gamma = \gamma_2 - \gamma_1$. Here, we used an in-plane isotropic $\varepsilon_{xx,\infty} = \varepsilon_{yy,\infty}, \varepsilon_{xy,\infty} = 0$ (which is different from $CdWO_4$) for the permittivity at the infinite frequency ($\omega \to \infty$) to remove the influence of permittivity tensor due to the additional implicit anisotropic polarization at the infinite frequency. In this way, we can simply vary the relative orientation angle as well as the damping term of each considered phonon modes to investigate their contributions to the asymmetry observed in our experiments. In Figure 1, we have changed the γ_2 to see how the non-orthogonality of induced polarization could affect the propagation of polaritons in the interface. We found the larger symmetry when $\gamma_2 = 60°$. In Figure 4, we aim to discuss how the polariton asymmetry could be further pronounced via modifying the loss, we keep $\gamma_2 = 60°$ and modify the damping frequency of first phonon resonance (the parameter S_1 in φ_1 term).

Note 3: The passivity bound in the permittivity tensor

Now we discuss the passivity condition. Under the time convention of $e^{-i\omega t}$, the passivity requires that imaginary part of diagonal terms must be positive, i.e. $Im(\varepsilon_{xx})>0$, $Im(\varepsilon_{yy})>0$, and $Im(\varepsilon_{zz})>0$. For the off-diagonal terms of permittivity tensors in monoclinic crystals shown in Equation (1.a), we have $Im(\varepsilon_{xx})*Im(\varepsilon_{yy}) \geq Im(\varepsilon_{xy})*Im(\varepsilon_{xy})$. One interesting consequence is that the imaginary part of off-diagonal terms can also be negative, which does not break the passivity condition[3].

Note 4: Polarization-resolved reflectance measurements

Polarization-dependent infrared reflectance measurements were performed using a FTIR microscopy (Thermo Fisher Nicolet). We generate a background spectrum on Au substrate for each polarization angle. The incident angle of light is near 30°. By rotating the polarizer plate a full round (separated by 30 degrees), the characteristic reflectance can be recorded at each polarization and indicate the relative direction of in-plane optic axis at each RBs.

Note 5: Further analysis on the origin of all phonon resonance.

For the reststrahlen band (RB) we observed in experiments, the next nearest RB range is close to be orthogonal to this one. This is reflected by the orientation angle of RB 1 and 2, correspondingly, in the table 1. As a matter of the fact, there are other factors that will also contribute to the asymmetry, majorly the (i) low-frequency phonon resonances (other RB range in the table) and (ii) high-frequency anisotropic response. Note the factor (ii) is because the permittivity tensor at $f \to \infty$ (i.e. $\bar{\bar{\varepsilon}}_\infty$ term) can give the additional polarization that is not parallel or perpendicular to RB1 or RB2. To further analyze these two factors, we consider the following three cases:

(a). the permittivity tensor that only has the exact phonon resonance RB1, and assume $\varepsilon_{xx,\infty} = \varepsilon_{yy,\infty} = 4.5$; $\varepsilon_{xy,\infty} = 0$. In this case, the factor (i) and (ii) are both gone, and the polaritons should be symmetric.

(b). the permittivity tensor that only has the exact phonon resonance RB1, and, and the realistic $\bar{\bar{\varepsilon}}_{\infty}$ component ($\varepsilon_{xx,\infty} = 4.46$, $\varepsilon_{yy,\infty} = 4.81$, $\varepsilon_{xy,\infty} = 0.086$). In this case, since the orientation of induced polarization from the factor (ii) is considered, while there is no factor (i).

(c). the realistic case where non-diagonal $\bar{\bar{\varepsilon}}_{\infty}$ term ($\varepsilon_{xx,\infty} = 4.46$, $\varepsilon_{yy,\infty} = 4.81$, $\varepsilon_{xy,\infty} = 0.086$) and all phonon resonances are considered.

We used the finite element method in the simulation with the commercially available software COMSOL Multiphysics. We used a z-oriented dipole at 200nm of the top of interface to excite the highly confined polaritons and collect the signals (real part of Ez) at the 50nm top of interface.

The results of following three cases are shown in Supplementary Figure 5, from panel a to c, respectively. The panel a is symmetric. Although the asymmetry in panel b and c is weak, it is still observable. To add the visual guide, we put two reference lines (marked as ① and ②, see green arrowed lines in top panels of Figure 5) along which the energy flows. It can be seen, around these two lines, the field patterns are not identical and there is the increased asymmetry. The asymmetry in panel b is due to the induced polarization from the contribution of $\bar{\bar{\varepsilon}}_{\infty}$ that is not along the first phonon resonance. The asymmetry in panel c is due to both the induced polarization from both the $\bar{\bar{\varepsilon}}_{\infty}$ term and the low-frequency phonon modes that are not along or perpendicular to that of first phonon resonance.

Section 2: The dispersion of low-symmetry bulk crystals

We can solve the Maxwell equations to obtain the dispersion of waves in the monoclinic crystals. In general, for the mode at the frequency ω with momentum (k_x, k_y, k_z), we should have the dispersion

$$\vec{k}\left(\vec{k}\cdot\vec{E}\right) - k^2\vec{E} + k_0^2\bar{\bar{\varepsilon}}\cdot\vec{E} = 0 \tag{2}$$

where $\vec{E} = \left[E_x, E_y, E_z\right]^T$.

The dispersion can thus be written as

$$\begin{aligned} &k_z^4\varepsilon_{zz} - k_z^2k_0^2\left[\varepsilon_{zz}\left(\varepsilon_{xx}+\varepsilon_{yy}\right)k_0^2 - \varepsilon_{zz}k_x^2 - \varepsilon_{zz}k_y^2 - \left(\varepsilon_{xx}k_x^2 + \varepsilon_{yy}k_y^2 + 2\varepsilon_{xy}k_xk_y\right)\right] \\ &\quad + \left(\varepsilon_{zz}k_0^2 - k_x^2 - k_y^2\right)\left[\varepsilon_{xx}\varepsilon_{yy}k_0^2 - \varepsilon_{xy}^2k_0^2 - \left(\varepsilon_{xx}k_x^2 + \varepsilon_{yy}k_y^2 + 2\varepsilon_{xy}k_xk_y\right)\right] = 0 \end{aligned} \tag{3}$$

as the solution of $\omega\left(k_x, k_y, k_z\right) = 0$ where $k_0 = \omega/c$, which also will give the corresponding eigen-modal distributions of $\left(E_x, E_y, E_z\right)$.

In general, the Equation (3) have two branch-cut solutions of k_z^2, corresponding to ordinary-like mode, usually less confined as dubbed k_{z1}^2, and extraordinary-like mode, usually highly confined as dubbed k_{z2}^2, in LSC. Each will again give two branch solutions of positive and negative

k_z, that will give $\pm k_{z1}$ and $\pm k_{z2}$. Here, when the momentum is large, the extraordinary mode will dominate, which is plotted in Supplementary Figure 9.

We now discuss how the low crystal symmetry will break the symmetry of the polaritons in physics and mathematics. For the orthorhombic system with off-diagonal terms, even if all permittivity can be complex-valued, one can rewrite the term of $\left(\varepsilon_{xx}k_x^2+\varepsilon_{yy}k_y^2+2\varepsilon_{xy}k_xk_y\right)$ as the $\left(\varepsilon_{x'x'}k_{x'}^2+\varepsilon_{y'y'}k_{y'}^2\right)$. Mathematically, this is equivalent to diagonalize the permittivity tensor in the new orthogonal spatial coordinate x' and y'. With this, one can clearly see that $\omega\left(+k_{x'},+k_{y'},\pm k_z\right)=\omega\left(-k_{x'},+k_{y'},\pm k_z\right)=\omega\left(+k_{x'},-k_{y'},\pm k_z\right)=\omega\left(-k_{x'},-k_{y'},\pm k_z\right)$, indicating the mode is the same with respect to optic axis. However, for monoclinic systems where the non-Hermitian permittivity tensor cannot be diagonalized in the real spaces, one cannot write the term of $\left(\varepsilon_{xx}k_x^2+\varepsilon_{yy}k_y^2+2\varepsilon_{xy}k_xk_y\right)$ as the $\left(\varepsilon_{x'x'}k_{x'}^2+\varepsilon_{y'y'}k_{y'}^2\right)$ in any Cartesian coordinates, or in the other words, one can never remove the term of product of $\varepsilon_{xy}k_xk_y$. Therefore, $\omega\left(+k_x,+k_y,k_z\right)\neq\omega\left(+k_x,-k_y,k_z\right)\neq\omega\left(-k_x,+k_y,k_z\right)$ along the effective optic axis, although that $\omega\left(k_x,k_y,k_z\right)=\omega\left(-k_x,-k_y,-k_z\right)$ due to the reciprocity. Hence, the solution of Equation (3) will not be identical with the respect to any effective optic axis, that underpins the low-symmetry polaritons (see next section for condition of the resonant surface modes).

With this, we can then define the mathematical quantitative $\mathcal{M}$ factor (see Methods) to measure the asymmetry, via essentially comparing the term of $\left(\varepsilon_{xx}k_x^2+\varepsilon_{yy}k_y^2+2\varepsilon_{xy}k_xk_y\right)$ as $\left(\varepsilon_{x'x'}k_{x'}^2+\varepsilon_{y'y'}k_{y'}^2\right)$ where the permittivity tensor is diagonalized in the coordinate x' and y'.

Section 3: Calculation of reflection and measured polaritonic modes

Here, we present the theory to calculate the reflectivity. We consider the in-plane momentum as (k_x,k_y). We consider the simple air-$CdWO_4$ interface, where $CdWO_4$ crystal locates at $z<0$ while air locates at $z>0$. We write the field in the air as both transverse electric mode (TE, s-wave) and transverse magnetic mode (TM, p-wave). This is given as $\vec{E}_s^{\pm}=\begin{bmatrix}k_y\\-k_x\\0\end{bmatrix}e^{-i\omega t+i\left(k_xx+k_yy\right)\pm ik_z^dz}$ and $\vec{E}_p^{\pm}=\begin{bmatrix}-k_x\\-k_y\\\frac{k_x^2+k_y^2}{k_z^d}\end{bmatrix}e^{-i\omega t+i\left(k_xx+k_yy\right)\pm ik_z^dz}$ where the positive and minus signs correspond to the momentum associated with (k_x,k_y,$\pm k_z^d$). Here, $k_z^d=\sqrt{\varepsilon_dk_0^2-k_x^2-k_y^2}$ and $\varepsilon_d=1$ for air side. The eigenmode in $CdWO_4$ is given by Equations (2) and (3). With this, we assume the incident light with p-wave, and calculate the reflection coefficient of p-wave by mapping the boundary conditions at the interface. Finally, we can write the reflection coefficient as

$$R_{pp}=\frac{\left[-k_z^d\frac{\varepsilon_{zz}}{\varepsilon_d}+k_x\gamma_{x1}+k_y\gamma_{y1}\right]\left(k_x\gamma_{y2}-k_y\gamma_{x2}\right)\left(k_{z2}+k_z^d\right)-\left[-k_z^d\frac{\varepsilon_{zz}}{\varepsilon_d}+k_x\gamma_{x2}+k_y\gamma_{y2}\right]\left(k_x\gamma_{y1}-k_y\gamma_{x1}\right)\left(k_{z1}+k_z^d\right)}{\left[k_z^d\frac{\varepsilon_{zz}}{\varepsilon_d}+k_x\gamma_{x1}+k_y\gamma_{y1}\right]\left(k_x\gamma_{y2}-k_y\gamma_{x2}\right)\left(k_{z2}+k_z^d\right)-\left[k_z^d\frac{\varepsilon_{zz}}{\varepsilon_d}+k_x\gamma_{x2}+k_y\gamma_{y2}\right]\left(k_x\gamma_{y1}-k_y\gamma_{x1}\right)\left(k_{z1}+k_z^d\right)}$$

where the $\gamma_{xj} = \frac{E_{xj}}{E_{zj}}$ and $\gamma_{yj} = \frac{E_{yj}}{E_{zj}}$ for j=1 and 2. Here, E_{xj}, E_{yj} and E_{zj} correspond to the eigen-field in $CdWO_4$ associated with momentum of k_{z1} and k_{z2} respectively, which can be found in solving Equations (2) and (3). This reflection coefficient gives the fitting of the FTIR in Supplementary Figure 2 and 3, as well as to calculate the resonant mode in air- $CdWO_4$ interface.

When momentum is large, which is usually true for highly confined modes, only one mode in the $CdWO_4$ is usually highly confined (with the momentum k_{z2}), while the other one is weakly confined and hence could be neglected for a clearer picture. For TM incidence, we define the transverse wave impedance of the background dielectrics as the ratio of tangent components $\eta_d = \frac{E_{tang}}{H_{tang}} = \eta_0 \frac{k_z^d}{k_0 \varepsilon_d}$, where $\eta_0 = \sqrt{\frac{\mu_0}{\varepsilon_0}}$ is the impedance of free space. In the $CdWO_4$ and neglecting the weakly confined mode, one can easily derive this transverse impedance can be written as $\eta_C \approx -\eta_0 \frac{\varepsilon_{zz} - k_x^2 - k_y^2}{\varepsilon_{zz} k_{z2} k_0}$. Hence, we can obtain the reflection coefficients as

$$R_{pp} = \frac{-\eta_d + \eta_C}{\eta_d + \eta_C}$$

where the resonant mode at the surface requires that the impedance to satisfy $\eta_d + \eta_C = 0$. For a mode (k_x, k_y) when $k_x^2 + k_y^2$ is constant, $\eta_d \propto k_z^d = \sqrt{\varepsilon_d k_0^2 - k_x^2 - k_y^2}$ will be the same. However, since $\eta_C \propto \frac{\varepsilon_{zz} - k_x^2 - k_y^2}{\varepsilon_{zz} k_{z2} k_0}$ (inversely proportional to k_{z2}) and the solution of k_{z2} given by Eq. (3) strongly depends on the choice of (k_x, k_y) even if $k_x^2 + k_y^2$ is constant (see Figure 4 in main text and in Supplementary Section 2), η_C will become different and depend on the specific mode of (k_x, k_y). As a result, this induces the asymmetric impedance matching that causes the asymmetric propagation of modes with respect to any effective axes at the surface. To put it more specifically, for a trial solution ($k_{x'}$, $k_{y'}$) that satisfies the impedance of $\eta_d + \eta_C = 0$, its mirror points with respect to any optical axes (-$k_{x'}$, $k_{y'}$) or ($k_{x'}$, - $k_{y'}$) will not satisfy this impedance condition due to different value of k_{z2} at those two points.

To extend the discussion and as a summary and with the establishment of impedance condition $\eta_d + \eta_C = 0$, we make the following statements.

Firstly, if there is no damping involved or we only consider the real permittivity, the mode we observe should be mirror symmetric. To justify, if there is no damping involved (we consider all entries are real), the symmetric permittivity matrix can be diagonalized via an orthonormal matrix Q, i.e. we can find that $Q\bar{\bar{\varepsilon}}Q^T$ is a diagonal matrix with real-valued numbers in the diagonal part. This orthonormal matrix Q (can be written as a unitary rotation matrix with respect to z axis in our case) can define a new orthogonal basis, such as (x', y', z). We further write the wavevector $\vec{k}$ in the new basis (denoted as $\vec{k}^Q = \left(k_x, k_y, k_z\right)^T = Q^T \vec{k}$) and will find that the solution of k_z in Eq. (1) would be the same if we solve it for $\left(\pm k_x, \pm k_y, k_z\right)$. This is because that the term of $\varepsilon_{xx} k_x^2 + \varepsilon_{yy} k_y^2 + 2\varepsilon_{xy} k_x k_y$ will become $\varepsilon_{x'} k_{x'}^2 + \varepsilon_{y'} k_{y'}^2$, while $k_x^2 + k_y^2 = k_{x'}^2 + k_{y'}^2$ due to the unitary transformation that conserves the quantity in Eq. (3). The solution of k_z in the crystal will then be symmetric with resect to the x' and y' axis, thus inducing the symmetric impedance matching condition. This is the equivalent to a lossless biaxial crystal.

Secondly, the non-Hermitian permittivity tensor is a necessary but not a sufficient condition for symmetry-broken polaritons we observed. To prove the necessity, we can first assume that the permittivity tensor would be a Hermitian permittivity tensor. In our case, this tensor is also symmetric according to the bound of reciprocity. Hence, the permittivity tensor would be real-valued. Therefore, this mode we observed must give a mirror symmetric feature according to the first statement. Hence, the non-Hermitian permittivity tensor is a necessary condition for symmetry-broken polaritons we observed. To prove the insufficient condition, we consider a non-Hermitian permittivity tensor that is zero in off-diagonal term but the same complex non-zero value in diagonal term (this hence denote an isotropic material), the mode would be symmetric obviously. An example is the surface plasmon polaritons in Au film which has equal propagation constant and decaying features along different directions.

Last, if all phonon resonances or polarization are orthogonal or parallel, the mode we observe would be mirror symmetric too. It is regardless of the hermicity or not of permittivity. This actually is a case of common biaxial crystal or uniaxial crystal, which has high crystal symmetry (such as hexagonal, triagonal, and tetragonal crystals) or orthorhombic crystal symmetry. To prove this statement, we can write the permittivity tensor in the basis defined by these orthogonal axes. Therefore, the off-diagonal permittivity component would be zero. With this, the Eq. (3) can be written as

$$\begin{aligned} k_z^4\varepsilon_{zz} - k_z^2k_0^2\left[\varepsilon_{zz}\left(\varepsilon_{xx}+\varepsilon_{yy}\right)k_0^2 - \varepsilon_{zz}k_x^2 - \varepsilon_{zz}k_y^2 - \left(\varepsilon_{xx}k_x^2+\varepsilon_{yy}k_y^2\right)\right] \\ +\left(\varepsilon_{zz}k_0^2 - k_x^2 - k_y^2\right)\left[\varepsilon_{xx}\varepsilon_{yy}k_0^2 - \left(\varepsilon_{xx}k_x^2+\varepsilon_{yy}k_y^2\right)\right] = 0 \end{aligned} \quad (4)$$

Again, a particular solution of (k_x, k_y, k_z) of the bulk mode would automatically guarantee that $(k_x, -k_y, k_z)$, $(-k_x, k_y, k_z)$ and $(-k_x, -k_y, k_z)$ would also be the solution, with the same feature, even if ε_{xx}, ε_{yy} and ε_{zz} are complex.

To summarize, from those discussions, it is the most important whether we can find a unitary transformation (more specifically in our case of reciprocal media, this corresponds to the unitary rotation operation in real space) of the complex permittivity tensor ($\bar{\bar{\varepsilon}} = \bar{\bar{\varepsilon}}^T$) to a diagonal form. This is equivalently to say whether we can transform the $\varepsilon_{xx}k_x^2 + \varepsilon_{yy}k_y^2 + 2\varepsilon_{xy}k_xk_y$ to the term as $\varepsilon_{x'}k_{x'}^2 + \varepsilon_{y'}k_{y'}^2$ while simultaneously preserving that $k_x^2 + k_y^2 = k_{x'}^2 + k_{y'}^2$. If we can diagonalize the permittivity tensor using unitary rotation matrix and perform the rotation operation in real space above, the polaritons we observed would be mirror symmetric, with respect to x'z and y'z plane. Otherwise, if we cannot diagonalize the permittivity tensor using rotation matrix (or equivalently real matrix in our case) to a diagonal term, the polaritons we observed are not mirror symmetric and hence symmetry-broken.

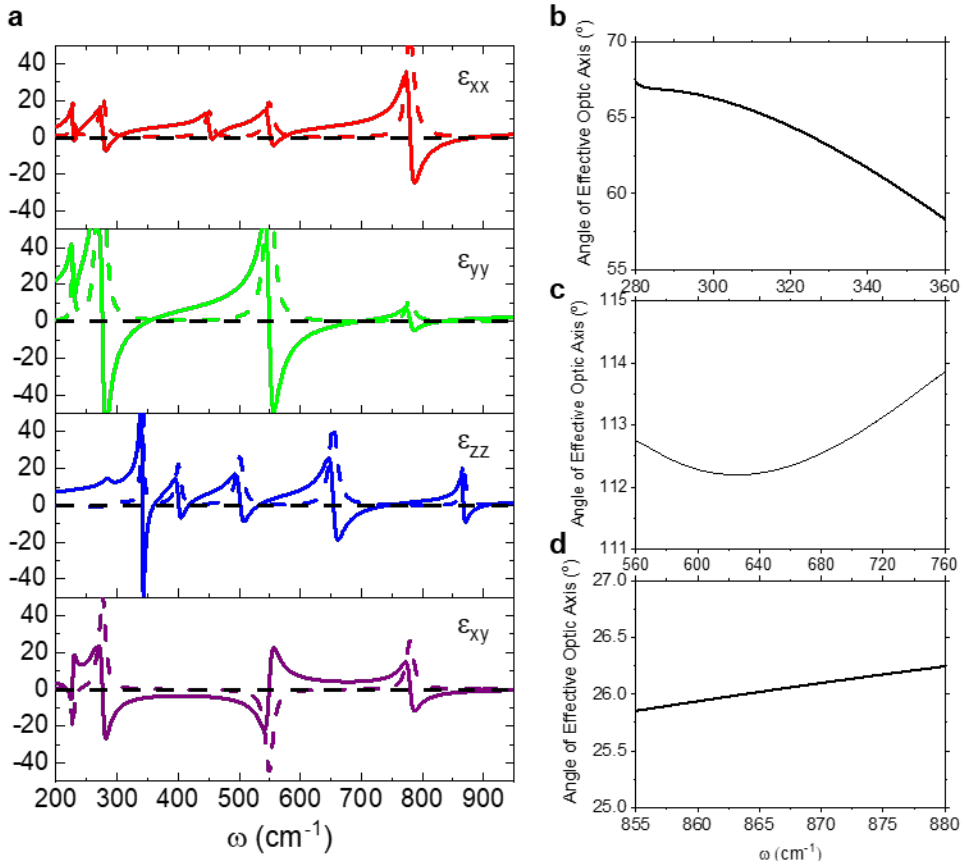

Supplementary Figure 1. The dielectric property of CdWO4. a, The four dielectric components of the permittivity tensor calculated by using the parameters shown in supplementary Table 1. Solid and dashed colored lines refers to the real and imaginary parts, respectively. Dashed black lines indicate the position of the zero value. **b**, The orientation angle of effective optic axis within the frequency range of 280-360 cm^{-1}. **c**, The orientation angle of effective optic axis within the frequency range of 560-760cm^{-1}. **d**. The orientation angle of effective optic axis within the frequency range of 855-880cm^{-1}.

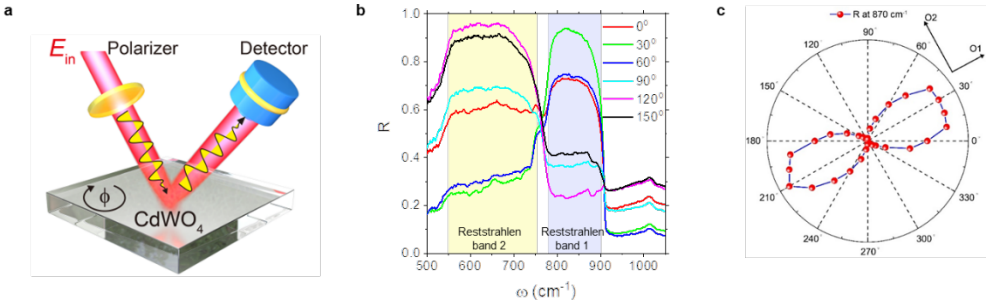

Supplementary Figure 2. **Polarization-resolved FTIR measurements for characterizing the rotary effective optic axis**. **a**, Sketch of the experimental set-up. The incident angle of the TM polarized illumination is around 30°. The principal direction angle φ of linear polarizer is rotated. **b**, Measured infrared reflectances under different angles. Two Reststrahlen bands (RB) associated in-plane optical phonons are revealed, i.e. the RB1 spanning from 779.5 cm^{-1} to 901 cm^{-1} (indicated by a purple shadow) and the RB2 from 549 cm^{-1} to 754 cm^{-1} (yellow shadow). **c**. Measured incident angular-resolved spectrum at the frequency 870 cm^{-1}.

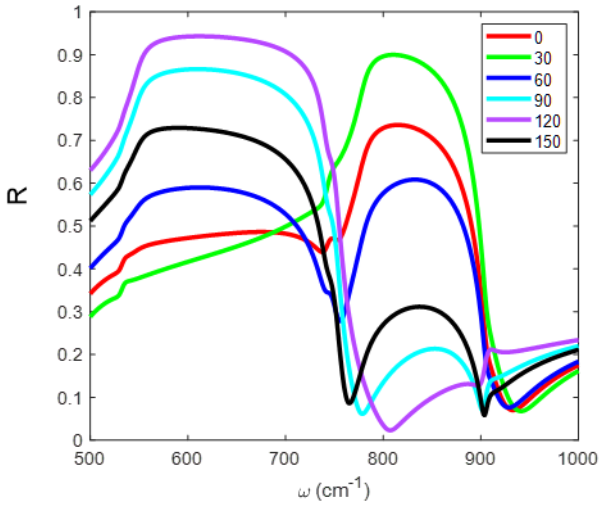

Supplementary Figure 3. The theoretical reflectance of polarization-resolved FTIR. The calculated reflectance for different orientation angles when rotating the sample. The incident angle of the TM-polarized illumination is set 25°.

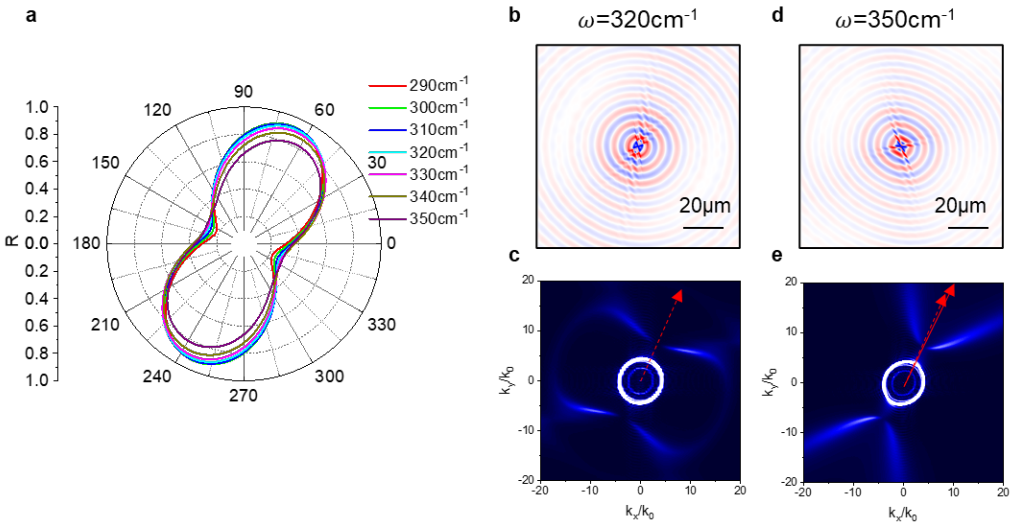

Supplementary Figure 4. Calculated anisotropic responses in the frequency range of 290-350 cm^{-1}. a, Calculated polar plots at different frequencies. **b,c**. Calculated near-field distribution [the component Re(E_z)] of dipole launched polaritons (panel **b**) at 320 cm^{-1} and the corresponding Fourier transform (panel **c**). **d,e**. Calculated near-field distribution [the component Re(E_z)] of dipole launched polaritons (panel **b**) at 350 cm^{-1} and the corresponding Fourier transform (panel **c**). Solid and Dashed red arrows in (**c** and **e**) indicate the O1 axis for 320 cm^{-1} and 350 cm^{-1}, respectively. The rotation of the O1 axis is caused by its notable dispersion with the same RB.

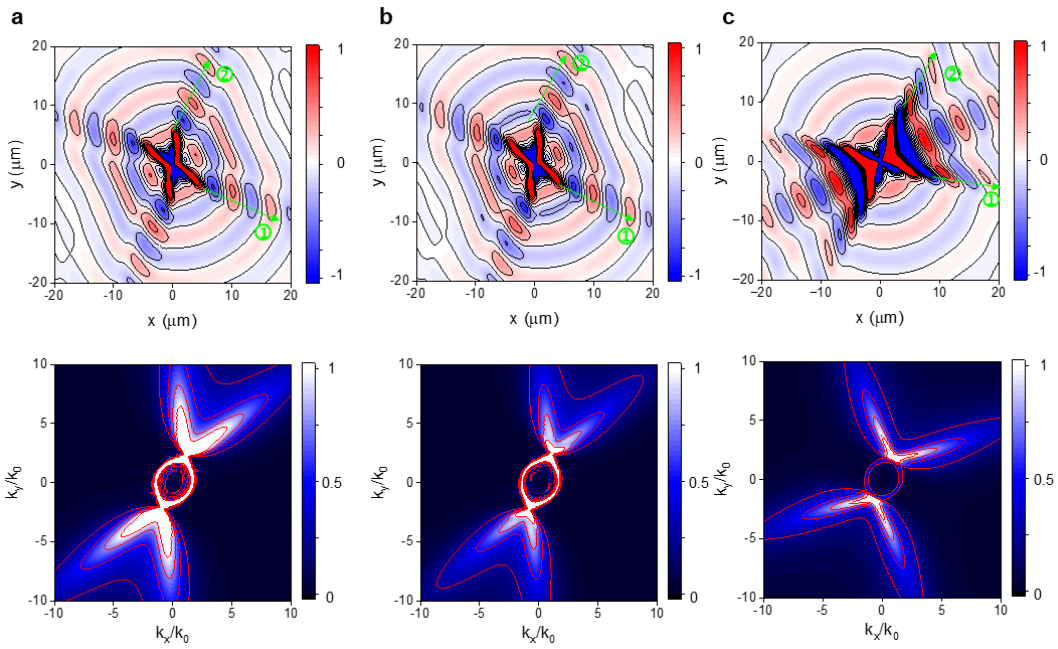

Supplementary Figure 5. The contounr with contour line plot of simulated fields (top panel) and its FT signals (bottom panel). **a**, The simulation with $\varepsilon_{xx,\infty} = \varepsilon_{yy,\infty} = 4.5$; $\varepsilon_{xy,\infty} = 0$ and only phonon resonance 1 of CdWO4. **b**, The simulation with $\varepsilon_{xx,\infty} = 4.46$, $\varepsilon_{yy,\infty} = 4.81$, $\varepsilon_{xy,\infty} = 0.086$ and the only the phonon resonance 1 of CdWO4. **c** The simulations in realistic cases where $\varepsilon_{xx,\infty} = 4.46$, $\varepsilon_{yy,\infty} = 4.81$, $\varepsilon_{xy,\infty} = 0.086$ and there are all phonon resonances. The green arrowed lines ① and ② along which the energy flows are added to annotate the asymmetry.

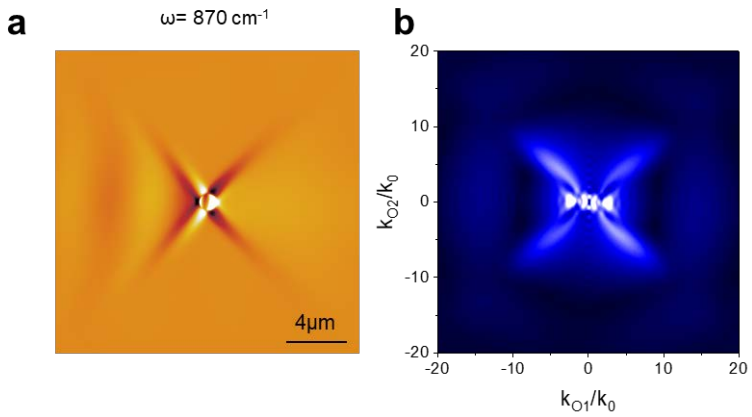

Supplementary Figure 6. Numerical simulations of antenna-launched polaritons at 870 cm^{-1}. a, Calculated near-field distribution**. b,** Fourier transform of the image shown in (a). In the numerical simulation, we use a *p*-polarized plane wave to illuminate the disk then acting an optical antenna to launch the polaritons. The illumination is well aligned along the O1 axis and incident angle is 30° relative to surface. The near-field distributions were recorded at a height of 50 nm above the surface. The simulation reproduces our experiments with excellent agreement, and the FT of the field distribution. Thus, the wavevector distribution also confirm the polariton asymmetry observed in experiments.

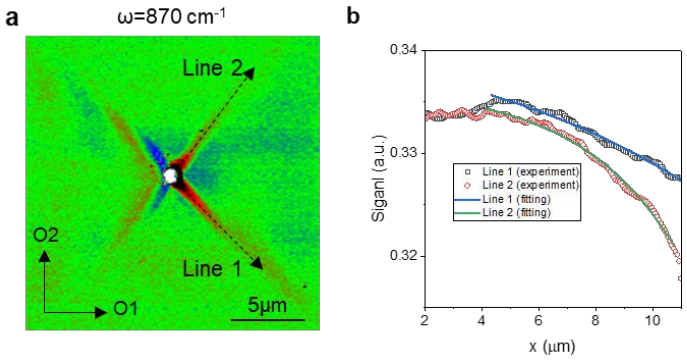

Supplementary Figure 7. The analysis of experimental signals. Before analysing the damping properties, we consider the the complex-valued optical signal σ after subtracting the background, the real part of the measured optical field (Re(σ)) can be calculated from the recorded amplitude (s(σ)) and phase (φ (σ)). Then the background signal (far from antenna) can be substrated by Re(σ) -Re(b), so that we get the nearly backgroud-free signal for further discussion. **a**. The measured experimental signals at $\omega = 870$ cm^{-1}. b. The fitting of measured signals along two major directions where the energy flows. The date of line 1 and 2 at the field along the lines 1 and 2 in panel b. We used the exponential decaying function ($y = A_0 e^{-x/\alpha} + A_1$) to fit where $1/\alpha$ is the decaying constant. We obtain that along line 1, $\alpha = 3.41 \pm 0.12$ μm and along line 2, $\alpha = 9.09 + 0.81$ μm.

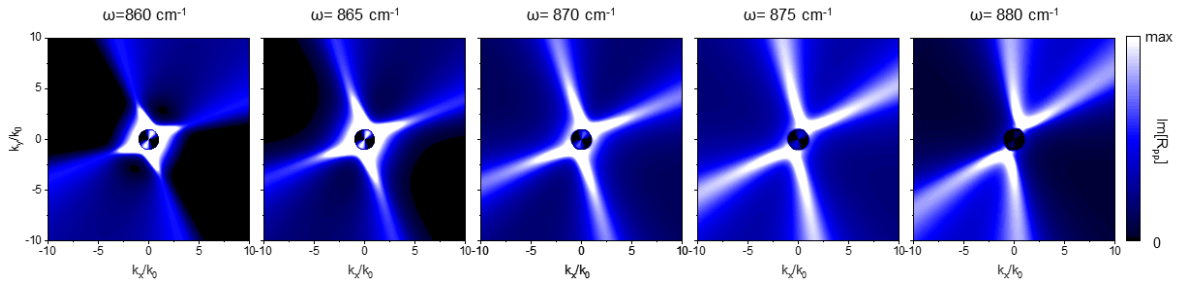

Supplementary Figure 8. Theoretically calculated in-plane hyperbolic polariton. From left to right, the working frequency changes from 860 to 880 cm^{-1}. These theoretical results agree well with the experimental data shown in Figure 1h and Figure 3e-h of the main text. The $\mathcal{M}$ value is 2.32E-5, 3.25E-5, 4.18E-5, 5.10E-5, 6.00E-5, respectively.

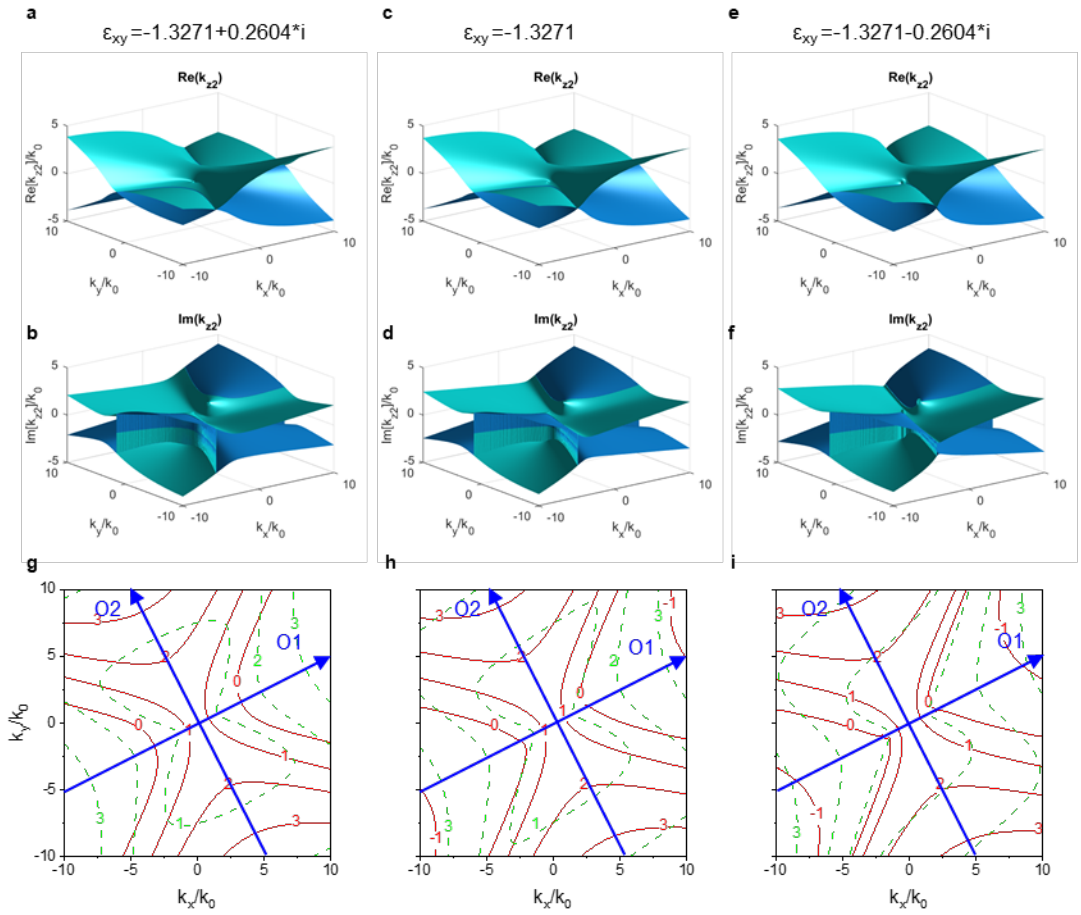

Supplementary Figure 9. The 3D dispersion of bulk $CdWO_4$. a,**b**. The real part (panel **a**) and imaginary part (panel **b**) of momentum along z-directions at ω=870 cm^{-1}. Here, permittivity at off-diagonal term ε_{xy}=-1.3271+0.2604*i. **c,d**. The real part (panel **c**) and imaginary part (panel **d**) of momentum along z-directions at ω=870cm^{-1}. Here, ε_{xy}=-1.3271. **e,f** The real part (panel **e**) and imaginary part (panel **f**) of momentum along z-directions at ω=870cm^{-1}. Here, ε_{xy}=-1.3271-0.2604*i. Other components are not changed. The cyan and blue surface denote the positive and negative signs of $\sqrt{k_{z2}^2}$ in the solution of Equation (3). **g-i.** The projection of k_z in kx-ky plane for the ε_{xy}=-1.3271+0.2604*i (panel **g**), ε_{xy}=-1.3271 (panel **h**) and ε_{xy}=-1.3271+0.2604*i (panel **i**). The red solid and green dashed contour lines mean the real and imaginary part of momentum along z direction at the associated position of (k_x, k_y), correspondingly. The blue solid arrows indicate the direction O1 and O2 of "effective" optic axis. The $\mathcal{M}$ values from panel **a-c** are 4.18E-5, 0.0223 and 0.0967, respectively.

Reference

1. Mock, A., Korlacki, R., Knight, S. and Schubert, M., Anisotropy, phonon modes, and lattice anharmonicity from dielectric function tensor analysis of monoclinic cadmium tungstate. *Phys. Rev. B* **95**, 165202 (2017)
2. Born, M. & Wolf, E. *Principles of Optics* 5th edn 333–334 (Pergamon, Oxford, 1975).
3. Mackay, Tom G., and Akhlesh Lakhtakia. *Electromagnetic anisotropy and bianisotropy: a field guide*. (2010).